A Journal of the Gesellschaft Deutscher Chemiker

Angewandte International Edition

GDCh

Chemie

www.angewandte.org

Accepted Article

Title: Polymethine-Based Semiconducting Polymer Dots with Narrow-Band Emission and Absorption/Emission Maxima at NIR-II for Bioimaging

Authors: Ming-Ho Liu, Zhe Zhang, Yu-Chi Yang, and Yang-Hsiang Chan

To be cited as: *Angew. Chem. Int. Ed.* 10.1002/anie.202011914

Link to VoR: https://doi.org/10.1002/anie.202011914

WILEY-VCH

10.1002/anie.202011914

WILEY-VCH

RESEARCH ARTICLE

Polymethine-Based Semiconducting Polymer Dots with Narrow-Band Emission and Absorption/Emission Maxima at NIR-II for Bioimaging

Ming-Ho Liu,[a†] Zhe Zhang,[b†] Yu-Chi Yang,[a] and Yang-Hsiang Chan*[ac]

[a] M.-H. Liu, Y.-C. Yang, Prof. Y.-H. Chan
Department of Applied Chemistry/Center for Emergent Functional Matter Science
National Chiao Tung University
Hsinchu, Taiwan 30050
[*] E-mail: yhchan@nctu.edu.tw
[†]Both authors contributed equally to this work
[b] Z. Zhang
Department of Biomedical Engineering
Southern University of Science and Technology
Shenzhen, Guangdong, China 518055
[c] Prof. Y.-H. Chan
Department of Medicinal and Applied Chemistry
Kaohsiung Medical University
Kaohsiung, Taiwan 80708

Supporting information for this article is given via a link at the end of the document.

Abstract: Deep-penetration fluorescence imaging in the second near-infrared (NIR-II) window heralds a new era of clinical surgery, in which high-resolution vascular/lymphatic anatomy and detailed cancerous tissues can be visualized in real time. Although several types of fluorescent agents, including inorganic nanostructures and small organic dyes have been extensively developed recently, only a few successful examples of NIR-II fluorescing polymers with much enhanced fluorescence brightness and photo/colloidal stability have been reported. Here we describe a series of polymethine-based semiconducting polymers with intrinsic emission maxima in the NIR-IIa (1300-1400 nm) window and absorption maxima ranging from 1082 to 1290 nm. We prepared these polymers as semiconducting polymer dots (Pdots) in aqueous solutions with fluorescence quantum yields of 0.05-0.18 %, and demonstrated their promising applications in noninvasive through-skull brain imaging in live mice with remarkable spatial resolution as well as signal-to-background contrast. This study offers a universal platform for future designing NIR-IIa or even NIR-IIb emitting Pdots.

Introduction

Biological imaging with various modalities can provide detailed observation of therapeutic and pathological processes to elucidate complicated molecular mechanisms underlying human diseases.[1] In particular, noninvasive fluorescence imaging appears to be the most versatile yet simple techniques and is able to offer unprecedented spatial and temporal resolutions with real-time monitoring ability.[2] The huge progress in clinical technology and instrumentation for fluorescence image-guided surgery in human patients in these years also makes this field, especially the development of highly emissive and biocompatible fluorophores, considerably highlighted and urgently demanded.[3]

As a key component of fluorescence imaging in clinical applications, the selection of contrast agent directly affects the precision of disease diagnosis and the treatment outcomes of patients. Fluorescence probes for in vivo studies are required to be highly bright, photostable, and biocompatible. Conventional small organic fluorophores, such as FDA-approved indocyanine green (ICG), methylene blue, and fluorescein, with emission in the visible to NIR-I (700-900 nm) windows, suffer from limited tissue penetration depth (< 3 mm) and strong tissue autofluorescence. This had hindered their wide adoption for clinical use. Identified merely several years ago, fluorescence imaging in the NIR-II (1000-1700 nm) region has been proved to have reduced photon absorption/scattering by biospecies and minimal background autofluorescence to afford deeper penetration depth with remarkable spatial resolution.[4] Enormous activities have been thereon focused on the development of various novel contrast agents, including single-walled carbon nanotubes,[5] rare-earth nanomaterials,[6] inorganic quantum dots,[7] and organic fluorophores.[3b, 3c, 8] Among these fluorescent probes, organic small molecules appear to be most attractive candidates for NIR-II imaging because of facile chemical synthesis, low cytotoxicity, and fast renal clearance in the body. However, there are still several unmet challenges of small molecule-based NIR-II probes including poor water dispersibility, low photostability, difficult functionalization, and more importantly, low fluorescence brightness (i.e., low extinction coefficient). To circumvent the aforementioned issues, usually phospholipids were employed to encapsulate these small dyes to generate lipid-based nanomicelles,[4b] while the known dye leaking phenomenon[9] and long-term in vivo optical stability remain a serious issue for further clinical translation. Additionally, it is synthetically difficult to obtain small organic molecules with absorption over 1100 nm and emission beyond 1300 nm owing to the extended conjugation scaffolds which are vulnerable especially in polar solvents. Therefore, serval reported works smartly utilized the emission tails (off-peak emission) of these NIR-II emitters to realize NIR-IIa (1300-1400 nm) or NIR-IIb (1500-1700 nm) imaging[3b, 3c, 10] but the spatiotemporal resolution must greatly rely on the CCD efficiency and adequate optical filters due to the low fluorescence brightness. Another strategy cleverly exploited *J*-aggregation of small dyes to bathochromically shift both their maximal absorption and emission into the desired windows.[4o, 11] In this scenario,

10.1002/anie.202011914

however, the significant aggregation-cased quenching (ACQ) behavior by 1-2 orders of magnitude is inevitable,[4o] which might constrain their widespread adoption.

In an effort to fundamentally tackle the above-mentioned persistent issues for small organic fluorophores, conjugated/semiconducting polymer-based nanoparticles thereby emerge as a unique solution for NIR-II fluorescence imaging. This type of nanoparticles, also abbreviated as Pdots/CPNs/SPNs, have multiple superior advantages over small organic molecules:[12] (i) ultrahigh fluorescence brightness due to the large absorption coefficient; (ii) excellent photostability; (iii) good water dispersibility and facile surface functionalization for targeting; (iv) large Stokes shift to avoid optical cross-talking; and (v) high biocompatibility. Unfortunately, to date, there is still a lack of Pdot with both absorption and emission maxima in the NIR-II window. This fact is dictated by the energy gap law that the nonradiative decays are accelerated by the vibrational overlap between the ground state and excited state due to the small energy gap.[13] Because of this intrinsic limitation, there is only a paucity of successful examples to acquire donor-acceptor type Pdots with emission in the NIR-II region although their absorption maxima are still in the NIR-I window and their fluorescence quantum yields are very low.[4h, 14]

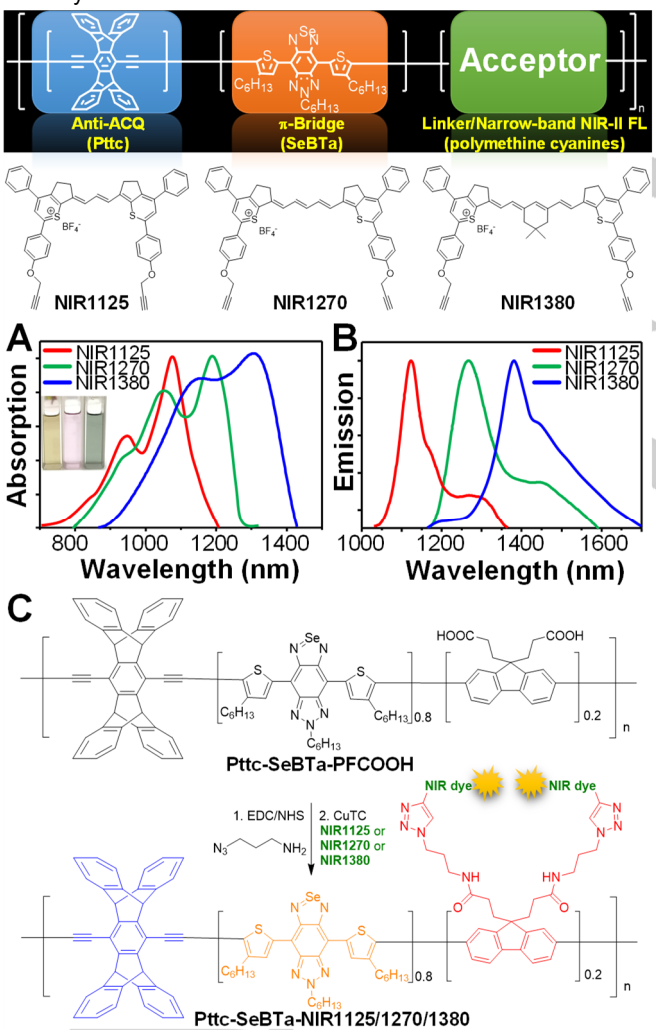

Figure 1. Chemical structures of polymethine dye-conjugated semiconducting polymers. Three types of NIR-II fluorescent polymethine dyes (NIR1125, NIR1270 and NIR1380) were synthesized with activable alkyne functional groups for further conjugation with the semiconducting polymer. (A) Absorption spectra of NIR1125 (red line), NIR1270 (green line), and NIR1380 (blue line) in CH_2Cl_2. The middle-left inset shows the photograph of the dye solutions. (B) Emission spectra of NIR1125 (red line), NIR1270 (green line), and NIR1380 (blue line) in CH_2Cl_2. (C) Synthesis of semiconducting polymer bearing carboxylic acid groups for further transformation to azide groups, followed by CuAAC click reactions with polymethine dyes.

The difficulty in getting Pdots with both absorption and emission in the NIR-II window has plagued almost all of the Pdot-related research communities for years. Herein, we successfully developed a novel yet universal platform to synthesize Pdots with narrow-band absorption and emission in the NIR-II region by integrating both advantages of small organic fluorophores and conjugated polymers. Specifically, we first synthesized a new type of semiconducting polymer with a bulky architecture to provide anti-aggregation-caused quenching (anti-ACQ) properties (Figure 1).[15] The rigid three-dimensional Pttc moieties as well as the bulky SeBTa units both contributed to effective steric hindrance to prevent ACQ phenomenon of post-linked NIR-II monomers. Here the fluorene derivatives on the polymer backbones simply offer azide functional groups to chemically bind alkyne-functionalized polymethine-cyanine dyes through copper(I)-catalyzed azide-alkyne cycloaddition (CuAAC) under mild conditions. In addition to the implantation of ani-ACQ characteristics to NIR-II dyes, the semiconducting polymers can at the same time strongly anchor the NIR-II fluorophores *via* robust chemical binding to preclude from the dye leaching issue encountered by small-dye doped polymeric[9] or lipidic nanoparticles (*vide infra*). The dye leaking problem could result in inconsistent optical signals and potential cytotoxicity, particularly for *in vivo* imaging applications. Besides the anti-ACQ function of the π-bridge, SeBTa with the absorption peak at ~820 nm, can also serve as a light-harvesting fragment for *in vitro* cellular studies whereas the penetration depth is less concerned in cellular levels. For *in vivo* NIR-II imaging, the direct excitation on the emitters is competent to offer high image clarity and quality of deep anatomical features.

Results and Discussion

We first synthesized three types of NIR-II fluorescent polymethine dyes of different conjugation lengths of intermediate, NIR1125, NIR1270, and NIR1380 (see Supporting Information), with narrow-band emissions. The narrow-band emissions are advantageous for multiplexed imaging. These polymethine cyanine-dyes were endowed with activable alkynes for conjugation with polymers. Their absorption and emission spectra are shown in Figure 1A and 1B, respectively, in which all of absorption and emission maxima are beyond 1000 nm. It is noticeable that the absorption maximal peak of NIR1380 locates at 1270 nm with its emission at 1380 nm (summarized in Table 1), which is beneficial for *in vivo* deep-tissue vascular imaging. We then synthesized a very bulky semiconducting polymer with anti-ACQ characteristics, Pttc-SeBTa-PFCOOH, to chemically bind with the polymethine dyes by click reactions (Figure 1C). This platform is universal that can be virtually used to integrate with all kinds of fluorophores with reactive alkynes.

Table 1. Summary of the Spectral Data of Polymethine Dyes in DCM

Monomer dyes	λ_{max}^{abs} (nm)[a]	λ_{max}^{em} (nm)[b]	Φ (%)[d]
NIR1125	936, 1066	1125	1.2
NIR1270	1050, 1188	1270	0.52
NIR1380	1140, 1270	1380	0.25

10.1002/anie.202011914

[a]Absorption maximum. [b]Emission maximum. [c]Fluorescnece Quantum yield.

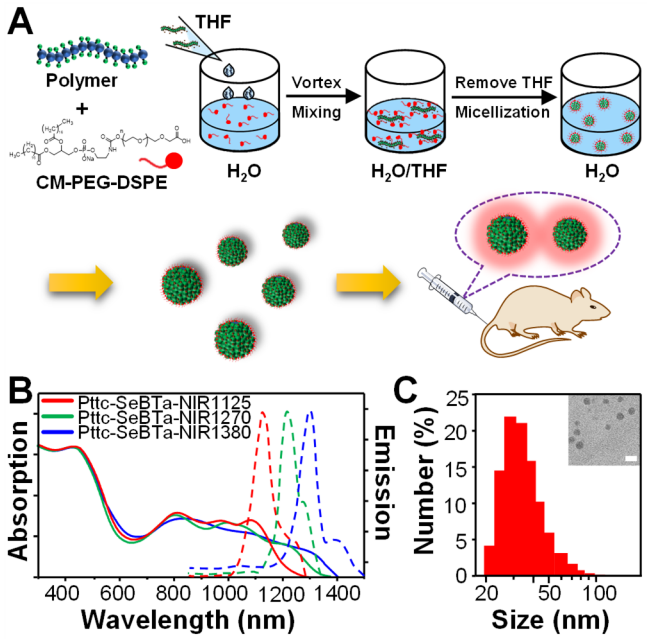

Figure 2. (A) Schematic showing the preparation of lipid-protected Pdots for *in vivo* bioimaging. (B) Absorption (solid lines) and fluorescence (dashed lines) spectra of Pttc-SeBTa-NIR1125 (red line), Pttc-SeBTa-NIR1270 (green lines), and Pttc-SeBTa-NIR1380 (blue lines) Pdots in aqueous solutions. The fluorescence data were obtained under 980 nm light excitation. (C) Representative hydrodynamic sizes of Pttc-SeBTa-NIR1125 Pdots measured by dynamic light scattering. The upper-right inset represents their corresponding TEM image with a scale bar of 50 nm.

The preparation of NIR-II Pdots was illustrated in Figure 2A where we used traditional nanoprecipitation method by co-precipitating amphiphilic lipids into Pdots to provide COOH functional groups for further surface engineering if needed. We found that Pttc-SeBTa-NIR1270 Pdots were optically unstable in aqueous solutions especially under light excitation while the Pttc-SeBTa-NIR1270 polymers were very stable in most organic solvents. This phenomenon is very similar to indocyanine green[16] with resembling chemical construction in which the mechanisms of the regioselective cleavage on the heptamethine cyanines by exogenously generated $^1O_2$ have been claimed experimentally and computationally.[3a, 17] On the other hand, NIR1125 and NIR1380 analogues exhibited high stability in organic solvents and in Pdot forms. We speculate that it is probably due to the shorter intermediate of NIR1125 and rigid center of NIR1380. The absorption and emission spectra of Pttc-SeBTa-NIR1125/NIR1270/NIR1380 Pdots were shown in Figure 2B. The absorption peaks at ~450 nm were attributed to the Pttc and polyfluorene segments. The peak at ~800 nm stemmed from the π-bridge units, SeBTa, while the broad peaks from 900 to 1400 nm were from the polymethine-cyanine monomers. It clearly indicates that these Pdots can be readily excited by several long wavelength lasers depending on the experimental requirement. The resulting Pdots possess the hydrodynamic diameters of 35-73 nm (Figure S3) and the typical distribution of hydrodynamic diameter of Ptt-SeBTa-NIR1125 Pdots along with their transmission electron microscope (TEM) image were displayed in Figure 2C.

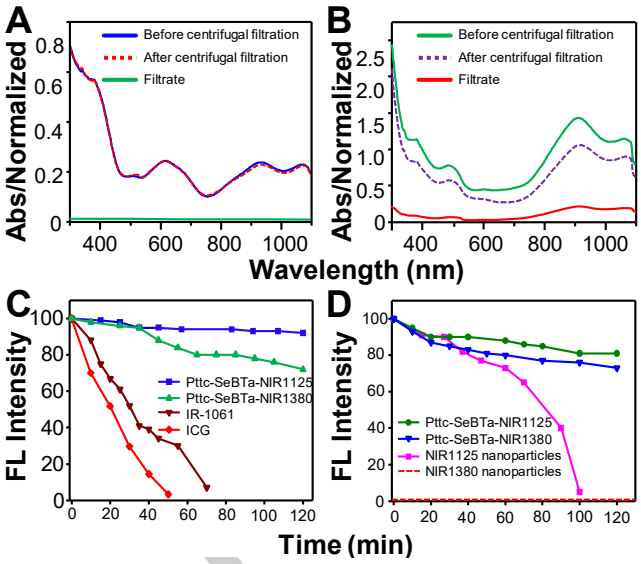

Figure 3. Evaluation of optical stability. (A) Absorption spectra of Pttc-SeBTa-NIR1125 Pdots before (solid blue line) and after (dashed red line) centrifugal filtration. The absorption spectrum of the filtrate (solid green line) indicates that no dye leaching phenomenon can be observed in the Pdot system. (B) Absorption spectra of small NIR1125 dye-doped lipid-based nanoparticles before (solid green line) and after (dashed purple line) centrifugal filtration. The absorption peaks of the filtrate (solid green line) suggests the significant dye leaching problem in the physical doping system. (C) Photostability (normalized fluorescence intensity vs irradiation time) of Pttc-SeBTa-NIR1125 Pdots in water (blue line), Pttc-SeBTa-NIR1380 Pdots in water (green line), IR-1061 dyes in CH_2Cl_2 (brown line), and ICG dyes in water (red line) under continuous 808 nm light irradiation (0.8 W/cm^2) at the same concentration of 200 pM. (D) Colloidal stability of Pttc-SeBTa-NIR1125 Pdots (solid green line), Pttc-SeBTa-NIR1380 Pdots (solid blue line), NIR1125 dye-doped lipid nanoparticles (solid pink line), and NIR1380 dye-embedded lipid nanoparticles (dashed red line) in DMEM cell culture media at 37 °C.

We further assessed the optical stability of the resulting Pdots. As shown in Figure 3A, a centrifugal filtration device with a 100 kDa molecular weight cut-off was used to concentrate Pttc-SeBTa-NIR1125 Pdots. The centrifugal filtration processes (for concentration or purification) were used to examine the optical stability of Pdots because these processes are necessary during the bioconjugation of Pdots for versatile biological applications. After the centrifugal filtration, the concentrated Pdots were diluted to the original volume by water and we found that the absorption of Pdots remained almost the same, indicating negligible leaching phenomenon for the covalently linked dyes. The minimal absorption of the filtrate also suggested that no dye leaking behavior could be observed. On the contrary, the commonly used lipid-based nanoparticles in which the small organic dyes were physically encapsulated into the lipid micelles, revealed the significant dye leaching issue as shown in Figure 3B. In this sample, small NIR1125 dyes were encapsulated into the DSPE lipid nanoparticles and the absorption intensity of NIR1125 dyes decreased after centrifugal filtration, implying the leaking of the embedded dyes from the polymer matrix. The obvious absorption of the filtrate further confirmed the leaching phenomenon. The above results suggested that the covalently dye-functionalized polymers possessed enhanced optical stability in comparison to the physically blended counterparts. In terms of photostability, an important photophysical property in bioimaging, Pttc-SeBTa-NIR1125 Pdots exhibited outstanding photostability under

10.1002/anie.202011914

continuous 808 nm light illumination (0.8 W/cm^2), in which their fluorescence remained over 90 % after 120 min of 808 nm light exposure as shown in Figure 3C. For Pttc-SeBTa-NIR1380 Pdots, the emission signal still remained nearly 70 % of their original intensity. On the other hand, small organic dyes such as IR-1061 and ICG, displayed significant photobleaching to less than 10 % of their original intensities in 70 min. These results clearly indicated the exceptional photostability of Pdots as compared to small organic fluorophores. We also evaluated the colloidal stability of Pdots in the cell culture media at 37 ºC to mimic the physiological conditions. As shown in Figure 3D, both Pttc-SeBTa-NIR1125 and Pttc-SeBTa-NIR1380 Pdots unveiled superior stability even after 2 h of incubation, while NIR1125 dye-embedded nanoparticles showed poor colloidal stability under the same conditions. It is worth mentioning that no fluorescence could be detected for NIR1380 dye encapsulated nanoparticles, probably due to the serious ACQ behaviors. This results again emphasized the importance of the employment of the bulky polymer skeletons.

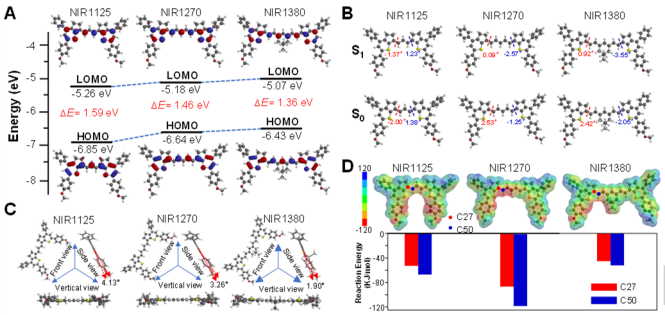

Figure 4. (A) Calculated HOMOs and LUMOs of the molecular fluorophores. (B) Optimized S_0 and S_1 geometries and the dihedral angles of these NIR-II fluorophores by density functional theory. (C) Multi-view images of optimized molecular geometries of NIR1125/NIR1270/NIR1380 in the ground state based on B3LYP/6-31G(d) level, showing the torsional angles between two thiopyrylium rings. (D) Maps of electrostatic potential surfaces of these dyes (upper panel) and computed reaction energies of two possible sites (C27 and C50) for cleavage reactions.

To further elucidate the influence of different intermediate lengths on the electronic energies and geometries of the fluorescent molecules, we executed time-dependent density functional theory (TDDFT) calculations at the B3LYP/6-31G(d) level using the Spartan software (the computational details were provided in the Supporting Information). Their highest occupied molecular orbitals (HOMOs) and lowest unoccupied molecular orbitals (LUMOs) are illustrated in Figure 4A. We can clearly observe that the extension of methine units effectively lowered the energy band gaps, leading to the redshifting in the both absorption and emission of the dyes of more than 200 nm (NIR1125 vs NIR1380). The HOMOs and LUMOs are delocalized over the polymethine backbones for all of the dyes. The partial separation of the LUMOs and HOMOs on the thiopyrylium (electron-donating group) and thiopyrylium salt (electron-withdrawing group) moieties accounted for intramolecular charge transfer between them. The optimized ground-state (S_0) and excited-state (S_1) geometries of these molecules were also plotted in Figure 4B. The dihedral angles between the thiopyrylium rings and polymethine chain are all smaller than 4º at both S_0 and S_1 states for all molecules, suggesting the low backbone distortion of these dyes. From the multi-view images as shown in Figure 4C, these molecules all exhibited good coplanar geometries along the polymethine chains. As the methine units extended from 5 (i.e., NIR1125) to 9 (i.e., NIR1380), the torsional angles (side view) between two thiopyrylium rings decreased from 4.13º to 1.90º, indicating the enhanced coplanar architectures along the p-conjugation backbones with the lengthening polymethine chains. Interestingly, we found that the central dimethylcyclohexene moiety of NIR1380 extended outwards the conjugated plane to provide the relatively large steric hindrance. The incorporation of steric hindrance on the polymethine chain is of importance to design stable polymethine fluorophores for bioimaging. The lack of steric hindrance on the extended polymethine chain (e.g., NIR1270) would result in the serious C-C oxidative cleavage under exposure to nucleophiles as mentioned above. This phenomenon could also explain for the excellent photostability of NIR1380 even with the longest conjugation length among these fluorophores, while NIR1270 appeared to possess very low photostability. The strategies designed to increase the stability and decrease photobleaching of polymethine dyes in aqueous media have recently be nicely reviewed by Zhang's group,[18] in which the conclusions are consistent with our results here. It is worth mentioning that the commercially available NIR-II dyes, IR-26, IR-1061, and IR-1048, each has a chlorocyclohexene unit on the center of its backbone (without the dimethyl moieties) and an even shorter methine unit of 5. It was found that these dye-loaded phospholipid micelles were prone to rapid degradation in polar solvent.[19] This behavior highlights the uniqueness of our stable NIR1380. To better understand the stability of these fluorophores from the aspect of charge distribution in a molecule, we performed the maps of electrostatic potential on the molecular surfaces as shown in Figure 4D. The oxidative cleavage process on the polymethine backbone immediately after the formation of C(OO)C dioxetane unit on C27/C50 carbon atoms (plotted as red and blue, respectively) has been proved to be the major reaction pathway.[17] Electrostatic potential analysis reveals that the C27/C50 atoms of NIR1270 have the favorably negative electrostatic potential to form the dioxetane intermediate and subsequent cleavage. Altogether, we have experimentally and computationally confirmed the critical role of dimethylcyclohexene shielding segment. This information is very important for chemists to rationally design more stable polymethine-based fluorophores with NIR-IIa/IIb fluorescence for bioimaging.

The fluorescence quantum yields of the resulting Pdots were determined by using IR-1061 in CH_2Cl_2 as the reference. Instead of using IR-26 as the reference owing to the variations of its quantum yields on different reports,[4o, 8a, 14b] we used IR-1061 with a certified value of 0.59 % in CH_2Cl_2,[20] in which its quantum yield was carefully corrected for reabsorption and reemission under the excitation light at 925 nm. Pttc-SeBTa-NIR1125 Pdots exhibited a good quantum yield of 0.18 %, while Pttc-SeBTa-NIR1380 Pdots possessed a modest quantum yield of 0.05 % in aqueous solutions (Table S1). Even the fluorescence quantum yield of the Pdots might not be very high as compared to traditional NIR small dyes, their fluorescence brightness, however, showed 1-2 orders of magnitude higher than that of commonly used organic dyes (Table S2). Moreover, the fluorescence background from biological species in the NIR-II window is low to ensure the practical implantation of these Pdots for *in vivo* bioimaging.

10.1002/anie.202011914

WILEY-VCH

RESEARCH ARTICLE

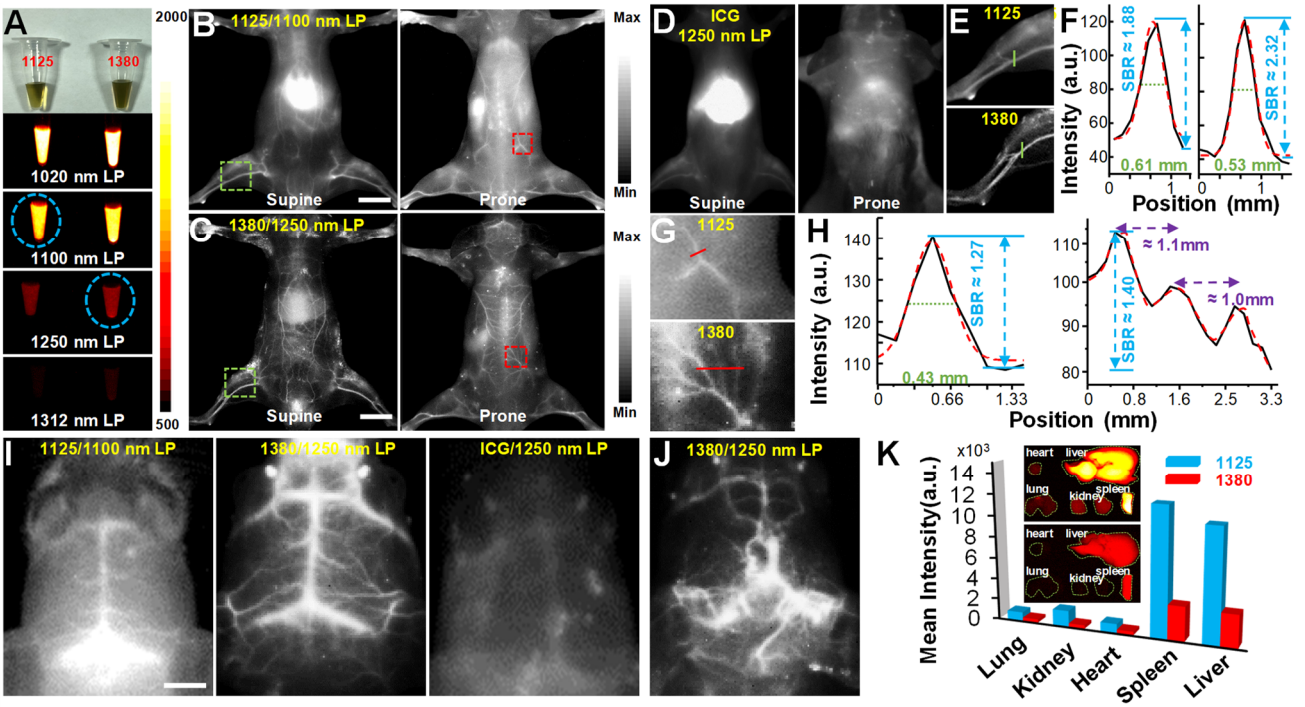

Figure 5. (A) Photographs of Pttc-SeBTa-NIR1125 (left) and Pttc-SeBTa-NIR1380 (right) Pdots under ambient light (first panel), and under 808 nm laser excitation with a 1020-nm long-pass filter (second panel), 1100-nm long-pass filter (third panel), 1250-nm long-pass filter (fourth panel), and 1312-nm long-pass filter (fifth panel). (B) Whole-body imaging of living mice intravenously injected by Pttc-SeBTa-NIR1125 Pdots in supine (left) and prone (right) positions with a 1100-nm long-pass filter. (C) Whole-body imaging of living mice intravenously injected by Pttc-SeBTa-NIR1380 Pdots in supine (left) and prone (right) positions with a 1250-nm long-pass filter. (D) Whole-body imaging of living mice intravenously injected by ICG in supine (left) and prone (right) positions with a 1250-nm long-pass filter. (E) The enlarged view of mouse hindlimb vasculature in the green squares of (B) (upper panel) and (C) (bottom panel), respectively. (F) Cross-sectional intensity profiles along the green lines in (E) for Pttc-SeBTa-NIR1125 (left) and Pttc-SeBTa-NIR1380 Pdots (right), respectively. (G) The enlarged view of the area close to the spinal cord in the red squares of (B) (upper panel) and (C) (bottom panel), respectively. (H) Cross-sectional intensity profiles along the red lines in (G) for Pttc-SeBTa-NIR1125 (left) and Pttc-SeBTa-NIR1380 Pdots (right), respectively. (I) NIR-II fluorescence imaging of wild-type C57BL/6 mouse brain vasculature after intravenous injection of Pttc-SeBTa-NIR1125 (left, 1100-nm long-pass filter), Pttc-SeBTa-NIR1380 (middle, 1250-nm long-pass filter) Pdots, and ICG (right, 1250-nm long-pass filter). (J) NIR-II fluorescence imaging of ND2:SmoA1 mouse brain vasculature after intravenous injection of Pttc-SeBTa-NIR1380 (1250-nm long-pass filter) Pdots. (I) Accumulation of Pttc-SeBTa-NIR1125 (upper panel in the inset) and Pttc-SeBTa-NIR1380 (bottom panel in the inset) Pdots in major excised organs at 24 h post-injection. Their corresponding quantitative mean fluorescence intensities were also plotted. The scale bars are 10 and 5 mm in B/C and I, respectively. The excitation power laser density was 5 mW/cm^2 with an exposure time of 800 ms. The mice were injected with 200 μL of Pdots (1.6 mg/mL) or ICG (200 μg/mL) *via* intravenous injection through. NIR-II imaging was performed after 10 min of post-injection For ICG experiments, all of the experimental conditions including laser power and filter sets were the same with Pttc-SeBTa-NIR1380 Pdots except that the acquisition time was 5 min of post-injection due to the fast renal clearance rate of ICG.

For biological applications, we first evaluated the cytotoxicity of Pdots by using MTT assays at different concentrations (Figure S5). The results revealed that minimal toxicity of Pdots in cells. We also performed the experiments of hepatotoxicity by intravenously injecting PBS and Pdots into the two separate mice. After 24 h post-injection, we measured the values of AST (aspartate aminotransferase; GOT, glutamate oxalacetate transaminase) and ALT (alanine aminotransferase; GPT, glutamate pyruvate transaminase) in serum to evaluate the liver function under Pdot treatment. Serum levels of AST at 24 h after injection were measured to be 129 and 76 U/L for PBS-treated and Pdot-treated mice, respectively. For the serum levels of ALT at 24 h after injection, they were determined to be 42 and 33 U/L for PBS-treated and Pdot-treated mice, respectively. Both values were in the normal ranges for PBS-treated or Pdot-treated mouse, indicating that the livers were still in normal function for both mice. We further carried out histological examination of livers by analyzing the H&E staining of liver tissues for both mice (Figure S6). The results suggest that Pdots have negligible hepatotoxicity. Before the *in vivo* non-invasive fluorescence imaging in mice, we examined the optical parameters of two types of Pdots with high stability which are suitable for bioimaging. As displayed in Figure 5A, we used a 808-nm laser with low excitation power (5 mW/cm^2) to minimize the photo-damage to mice as well as Pdots, and equipped with four different types of long-pass filters (1020, 1100, 1250, and 1312 nm). Although it was obvious to find that the use of a shorter long-pass filter (i.e., 1020 nm) appeared the highest fluorescence brightness, the spatial resolution and the signal-to-background ratio (SBR) for *in vivo* imaging presented the opposite way due to strong background interference.[3b, 4o, 14b] This means that the selection of a longer long-pass filter while keeping the high brightness is prerequisite. As a trade-off, we used a 1100-nm long-pass filter for Pttc-SeBTa-NIR1125 Pdots (traditional NIR-II) and a 1250-nm long-pass filter for Pttc-SeBTa-NIR1380 Pdots (NIR-IIb), respectively. We further executed whole-body fluorescence imaging in living mice by intravenously injecting these two Pdots separately into mice via the tail vein and compared their performance (Figure 5B-E). From Figure 5B-C, it can be clearly seen that the fluorescence imaging performed by Pttc-SeBTa-NIR1380 Pdots equipped with a 1250-nm long-pass filter revealed a significantly higher SBR as compared to the 1125 ones. On the contrary, the imaging resolution obtained by ICG appears to be very poor as shown in Figure 5D. From the enlarged view of the mouse hindlimb vasculature (Figure 5E), these two Pdots exhibited the similar spatial resolution of 0.53-0.61 mm while the Pttc-SeBTa-NIR1380 Pdots showed an enhanced SBR of 2.32, about 1.2 times higher than that of Pttc-SeBTa-NIR1125 Pdots (Figure 5F). These results further confirmed the advantages of NIR-IIb imaging with nearly zero autofluorescence and minimal photon scattering. Similarly, the

blood vessels nearby the spinal cord could also be easily visualized but the Pttc-SeBTa-NIR1380 Pdots offered a much higher resolution due to the low background interference (Figure 5G-H). It should be noted that the direct comparison of spatial resolution and SBR with other imaging platforms might be less scientifically important because these values depend highly on the quantum efficiency of CCD camera, the concentration of probes, imaging software, and the power/wavelength of the excitation light; rather than simply on the fluorescence brightness of the probes used. The cerebral blood vessels of mouse through intact scalp and skull could be distinctly delineated with fine vascular structures (Figure 5I) by taking the advantages of high penetration depth and minimized background interference in the NIR-II window. The sharp resolution of NIR-IIb imaging were again highlighted by the use of Pttc-SeBTa-NIR1380 Pdots (middle panel in Figure 5I). Benefiting from the ability of through-skull/scalp NIR-II imaging, we aim to the diagnose the malignant brain tumor in vivo from the vascular morphology in the mouse brain. Here we selected a ND2:SmoA1 transgenic mouse as the model because medulloblastomas in ND2:SmoA1 mice and humans have concomitant increase in certain signaling pathway activities for tumor survival and medulloblastoma is the most common type of malignant brain tumor that afflicts children. As shown in Figure 5J, the brain vasculature in the ND2:SmoA1 mouse exhibited a major area of structural disorder in the brain vasculature. On the other hand, the brain vasculature in the wild-type C57BL/6 mouse appeared to be orderly arranged and distributed in the brain. These results demonstrate that the deep-tissue NIR-II imaging presents to be a promising new technique for the early diagnosis of diseases associated with the brain blood vessel abnormality. The mice were further anatomized to analyze the Pdot distribution in major organs, where the fluorescence was found mostly in liver, kidney, and spleen (Figure 5K). The high accumulation of Pdots in liver and spleen suggested that the hepatobiliary clearance system was the main metabolic pathway of Pdots.

Conclusion

In summary, we have synthesized a new series of NIR-II fluorescent polymethine-based Pdots with narrow-band and NIR-II absorption/emission. The substantially higher optical and colloidal stability of these Pdots in comparison to small organic dyes and dye-doped lipid nanoparticles were demonstrated. *In vivo* non-invasive fluorescence imaging in mice with Pttc-SeBTa-NIR1125 (traditional NIR-II window) and Pttc-SeBTa-NIR1380 (NIR-IIb window) was performed and their spatial resolution and SBR were then compared, revealing the superior advantages of NIR-IIb imaging. Noteworthily, this platform is universal and can be readily adapted for versatile NIR-II fluorescent monomer to circumvent the intrinsic energy gap law of conjugated polymers. We believe this work will provide a footstone for future inspiration in refining current biological imaging technologies.

Acknowledgements

We would like to thank the MOST, Taiwan (grant No. 105-2113-M-110-012-MY3) and the Center for Emergent Functional Matter Science of National Chiao Tung University from The Featured Areas Research Center Program within the framework of the Higher Education Sprout Project by the Ministry of Education (MOE) in Taiwan.

Keywords: semiconducting polymers • NIR-II • narrow-band fluorescence • synthesis of Pdots • deep-tissue imaging

[1] aH.-W. Liu, L. Chen, C. Xu, Z. Li, H. Zhang, X.-B. Zhang, W. Tan, *Chem. Soc. Rev.* **2018**, *47*, 7140-7180; bB. R. Smith, S. S. Gambhir, *Chem. Rev.* **2017**, *117*, 901-986.
[2] aE. M. Sevick-Muraca, *Annu. Rev. Med.* **2012**, *63*, 217-231; bG. Hong, S. Diao, J. Chang, A. L. Antaris, C. Chen, B. Zhang, S. Zhao, D. N. Atochin, P. L. Huang, K. I. Andreasson, C. J. Kuo, H. Dai, *Nat. Photonics* **2014**, *8*, 723-730.
[3] aD.-H. Li, C. L. Schreiber, B. D. Smith, *Angew. Chem. Int. Ed.* **2020**, *59*, 2-10; bY. Li, Z. Cai, S. Liu, H. Zhang, S. T. H. Wong, J. W. Y. Lam, R. T. K. Kwok, J. Qian, B. Z. Tang, *Nat. Commun.* **2020**, *11*, 1255; cY. Li, Y. Liu, Q. Li, X. Zeng, T. Tian, W. Zhou, Y. Cui, X. Wang, X. Cheng, Q. Ding, X. Wang, J. Wu, H. Deng, Y. Li, X. Meng, Z. Deng, X. Hong, Y. Xiao, *Chem. Sci.* **2020**, *11*, 2621-2626.
[4] aH. Wan, H. Du, F. Wang, H. Dai, *Adv. Funct. Mater.* **2019**, *29*, 1900566; bKenry, Y. Duan, B. Liu, *Adv. Mater.* **2018**, *30*, 1802394; cX. Dang, L. Gu, J. Qi, S. Correa, G. Zhang, A. M. Belcher, P. T. Hammond, *Proc. Natl. Acad. Sci. U. S. A.* **2016**, *113*, 5179-5184; dD. Kobat, N. G. Horton, C. Xu, *J. Biomed. Opt.* **2011**, *16*, 106014; eF. Wang, H. Wan, Z. Ma, Y. Zhong, Q. Sun, Y. Tian, L. Qu, H. Du, M. Zhang, L. Li, H. Ma, J. Luo, Y. Liang, W. J. Li, G. Hong, L. Liu, H. Dai, *Nat. Methods* **2019**, *16*, 545-552; fQ. Yang, Z. Hu, S. Zhu, R. Ma, H. Ma, Z. Ma, H. Wan, T. Zhu, Z. Jiang, W. Liu, L. Jiao, H. Sun, Y. Liang, H. Dai, *J. Am. Chem. Soc.* **2018**, *140*, 1715-1724; gG. Hong, S. Diao, A. L. Antaris, H. Dai, *Chem. Rev.* **2015**, *115*, 10816-10906; hG. Hong, Y. Zou, A. L. Antaris, S. Diao, D. Wu, K. Cheng, X. Zhang, C. Chen, B. Liu, Y. He, J. Z. Wu, J. Yuan, B. Zhang, Z. Tao, C. Fukunaga, H. Dai, *Nat. Commun.* **2014**, *5*, 4206; iB. Li, L. Lu, M. Zhao, Z. Lei, F. Zhang, *Angew. Chem. Int. Ed.* **2018**, *57*, 7483-7487; jR. Tian, H. Ma, Q. Yang, H. Wan, S. Zhu, S. Chandra, H. Sun, D. O. Kiesewetter, G. Niu, Y. Liang, X. Chen, *Chem. Sci.* **2019**, *10*, 326-332; kS. He, J. Song, J. Qu, Z. Cheng, *Chem. Soc. Rev.* **2018**, *47*, 4258-4278; lY. Fan, P. Wang, Y. Lu, R. Wang, L. Zhou, X. Zheng, X. Li, J. A. Piper, F. Zhang, *Nat. Nanotechnol.* **2018**, *13*, 941-946; mF. Ding, Y. Fan, Y. Sun, F. Zhang, *Adv. Mater.* **2019**, *8*, 1900260; nZ. Lei, C. Sun, P. Pei, S. Wang, D. Li, X. Zhang, F. Zhang, *Angew. Chem. Int. Ed.* **2019**, *58*, 8166-8171; oC. Sun, B. Li, M. Zhao, S. Wang, Z. Lei, L. Lu, H. Zhang, L. Feng, C. Dou, D. Yin, H. Xu, Y. Cheng, F. Zhang, *J. Am. Chem. Soc.* **2019**, *141*, 19221-19225; pJ. Li, K. Pu, *Chem. Soc. Rev.* **2019**, *48*, 38-71; qJ. Cao, B. Zhu, K. Zheng, S. He, L. Meng, J. Song, H. Yang, *Front. Bioeng. Biotechnol.* **2020**, *7*, 487.
[5] K. Welsher, Z. Liu, S. P. Sherlock, J. T. Robinson, Z. Chen, D. Daranciang, H. Dai, *Nat. Nanotechnol.* **2009**, *4*, 773-780.
[6] Y. Zhong, Z. Ma, S. Zhu, J. Yue, M. Zhang, A. L. Antaris, J. Yuan, R. Cui, H. Wan, Y. Zhou, W. Wang, N. F. Huang, J. Luo, Z. Hu, H. Dai, *Nat. Commun.* **2017**, *8*, 737.
[7] L.-Y. Huang, S. Zhu, R. Cui, M. Zhang, *Anal. Chem.* **2020**, *92*, 535-542.
[8] aB. Ding, Y. Xiao, H. Zhou, X. Zhang, C. Qu, F. Xu, Z. Deng, Z. Cheng, X. Hong, *J. Med. Chem.* **2019**, *62*, 2049-2059; bF. Ding, Y. Zhan, X. Lu, Y. Sun, *Chem. Sci.* **2018**, *9*, 4370-4380.
[9] J. Yu, C. Wu, X. Zhang, F. Ye, M. E. Gallina, Y. Rong, I.-C. Wu, W. Sun, Y.-H. Chan, D. T. Chiu, *Adv. Mater.* **2012**, *24*, 3498-3504.
[10] S. Zhu, B. C. Yung, S. Chandra, G. Niu, A. L. Antaris, X. Chen, *Theranostics* **2018**, *8*, 4141-4151.
[11] P. Sun, Q. Wu, X. Sun, H. Miao, W. Deng, W. Zhang, Q. Fan, W. Huang, *Chem. Commun.* **2018**, *54*, 13395-13398.
[12] aC. Wu, D. T. Chiu, *Angew.Chem. Int. Ed.* **2013**, *52*, 3086-3109; bY.-H. Chan, P.-J. Wu, *Part. Part. Syst. Charact.* **2015**, *32*, 11-28; cK. Li, B. Liu, *Chem. Soc. Rev.* **2014**, *43*, 6570-6597; dK. Pu, A. J. Shuhendler, J. V. Jokerst, J. Mei, S. S. Gambhir, Z. Bao, J. Rao, *Nat. Nanotechnol.* **2014**, *9*, 233-239; eK. Pu, N. Chattopadhyay, J. Rao, *J. Control. Release* **2016**, *240*, 312-322; fX. Lim, *Nature* **2016**, *531*, 26-28; gL. Feng, C. Zhu, H. Yuan, L. Liu, F. Lv, S. Wang, *Chem. Soc. Rev.* **2013**, *43*, 6620-6633; hQ. Miao, C. Xie, X. Zhen, Y. Lyu, H. Duan, X. Liu, J. V. Jokerst, K. Pu, *Nat. Biotechnol.* **2017**, *35*, 1102-1110; iJ. Yu, Y. Rong, C.-T. Kuo, X.-H. Zhou, D. T. Chiu, *Anal. Chem.* **2017**, *89*, 42-56; jH.-S. Peng, D. T. Chiu, *Chem. Soc. Rev.* **2015**, *44*, 4699-4722; kY. Guo, Y. Li, Y. Yang, S. Tang, Y. Zhang, L. Xiong, *ACS Appl. Mater. Interfaces* **2018**, *10*, 20884-20896; lF. Ye, C. Wu, Y. Jin, Y.-H. Chan, X. Zhang, D. T. Chiu, *J. Am. Chem. Soc.* **2011**, *133*, 8146-8149; mY. Rong, C. W. J. Yu, X. Zhang, F. Ye, M. Zeigler, M. E. Gallina, I.-C. Wu, Y. Zhang, Y.-H. Chan, W. Sun, K. Uvdal, D. T. Chiu, *ACS Nano* **2013**, *7*, 376-384; nS.-Y. Kuo, H.-H. Li, P.-J. Wu, C.-P. Chen, Y.-C. Huang, Y.-H. Chan, *Anal. Chem.* **2015**, *87*, 4765-4771; oC.-T. Kuo, A. M. Thompson, M. E. Gallina, F. Ye, E. S. Johnson, W. Sun, M. Zhao, J. Yu, I.-C. Wu, B. Fujimoto, C. C. DuFort, M. A. Carlson, S. R. Hingorani, A. L. Paguirigan, J. P. Radich, D. T. Chiu, *Nat. Commun.* **2016**, *7*, 11468; pK. Sun, Y. Tang, Q. Li, S. Yin, W. Qin, J. Yu, D. T. Chiu, Y. Liu, Z. Yuan, X. Zhang, C. Wu, *ACS Nano* **2016**, *10*, 6769-6781; qK. Chang, Z. Liu, X. Fang, H. Chen, X. Men, Y. Yuan, K. Sun, X. Zhang, Z. Yuan, C. Wu, *Nano Lett.* **2017**, *17*, 4323-4329; rL. Wu, I.-C. Wu, C. C. DuFort, M. A.

10.1002/anie.202011914

Carlson, X. Wu, L. Chen, C.-T. Kuo, Y. Qin, J. Yu, S. R. Hingorani, D. T. Chiu, *J. Am. Chem. Soc.* **2017**, *139*, 6911-6918.
[13] aR. Englman, J. Jortner, *Mol. Phys.* **1970**, *18*, 145-164; bW.-C. Chen, P.-T. Chou, Y.-C. Cheng, *J. Phys. Chem. C* **2019**, *123*, 10225-10236.
[14] aK. Shou, Y. Tang, H. Chen, S. Chen, L. Zhang, A. Zhang, Q. Fan, A. Yu, Z. Cheng, *Chem. Sci.* **2018**, *9*, 3105-3110; bZ. Zhang, X. Fang, Z. Liu, H. Liu, D. Chen, S. He, J. Zheng, B. Yang, W. Qin, X. Zhang, C. Wu, *Angew. Chem. Int. Ed.* **2019**, *59*, 3691-3698.
[15] W.-K. Tsai, C.-I. Wang, C.-H. Liao, C.-N. Yao, T.-J. Kuo, M.-H. Liu, C.-P. Hsu, S.-Y. Lin, C.-Y. Wu, J. R. Pyle, J. Chen, Y.-H. Chan, *Chem. Sci.* **2019**, *10*, 198-207.
[16] J. T. Alander, I. Kaartinen, A. Laakso, T. Pätilä, T. Spillmann, V. V. Tuchin, M. Venermo, P. Välisuo, *Int. J. Biomed. Imaging* **2012**, *2012*, 940585.
[17] R. R. Nani, J. A. Kelley, J. Ivanic, M. J. Schnermann, *Chem. Sci.* **2015**, *6*, 6556-6563.
[18] B. Li, M. Zhao, F. Zhang, *ACS Materials Lett.* **2020**, *2*, 905-917.
[19] S. Wang, Y. Fan, D. Li, C. Sun, Z. Lei, L. Lu, T. Wang, F. Zhang, *Nat. Commun.* **2019**, *10*, 1058.
[20] R. Hoshi, K. Suzuki, N. Hasebe, T. Yoshihara, S. Tobita, *Anal. Chem.* **2020**, *92*, 607-611.

10.1002/anie.202011914

Entry for the Table of Contents

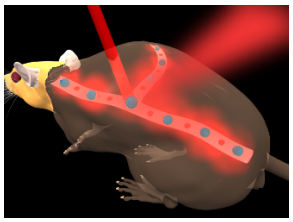

A novel series of polymethine-based semiconducting polymers were synthesized for the first time and prepared as Pdots in water with both absorption and emission in the NIR-II window. These Pdots can be further applied for deep-tissue non-invasive fluorescence imaging.